Journal of Materials Chemistry C

ROYAL SOCIETY OF CHEMISTRY

PAPER

View Article Online
View Journal | View Issue

Cite this: J. Mater. Chem. C, 2026, 14, 5005

Balancing charge transport and C–N bond strength in stability-oriented host design for blue TADF-OLEDs

Domantas Berenis,[a] Giedrius Puidokas,[a] Kristupas Bagdonas,[a] Goda Grybauskaitė,[a] Dovydas Banevičius,[a] Gediminas Kreiza,[a] Eigirdas Skuodis,[a] Rita Butkutė,[ab] Juozas V. Gražulevičius[b] and Karolis Kazlauskas*[a]

Achieving stable and efficient blue thermally activated delayed fluorescence (TADF) OLEDs remains a critical challenge due to high-energy excitons and polarons that induce bond cleavage in host materials, limiting operational lifetimes. Here, a series of carbazole–biphenyl hosts is developed with tuned charge transport from ambipolar to strongly electron-transporting, while maintaining relatively high triplet energies (2.77–2.85 eV in neat films), enabling the systematic probing of charge balance and degradation mechanisms in blue TADF-OLEDs. Incorporating blue TADF emitters of different triplet energies (2.79 eV and 2.62 eV) at optimized doping levels (7–40 wt%), the devices exhibit maximum external quantum efficiencies up to 18% with low efficiency roll-off for the most suitable host-dopant combinations. Operational stability assessments at 1000 cd m^{-2} reveal that, within the same device architecture and fabrication protocol, OLEDs using the *N*-phenylated host consistently outperform the non-phenylated analogues by 1.6–12 times in terms of LT_{50} lifetimes. Density functional theory calculations link this enhanced stability to the higher anionic-state bond dissociation energy (BDE) of the weakest exocyclic C–N bond (2.22 eV *vs.* 0.73–0.75 eV in the non-phenylated hosts), achieved by shifting LUMO density away from the carbazole core *via* *N*-phenyl substitution. These findings establish anionic-state C–N bond strength as a key molecular parameter for robust high-triplet-energy hosts, providing chemically grounded design guidelines to mitigate polaron-induced degradation while retaining efficiency under the studied device conditions.

Received 11th December 2025,
Accepted 28th January 2026

DOI: 10.1039/d5tc04350f

rsc.li/materials-c

1. Introduction

Thermally activated delayed fluorescence (TADF) has transformed the landscape of organic light-emitting diodes (OLEDs) by enabling the full utilization of both singlet and triplet excitons through reverse intersystem crossing (RISC) between nearly isoenergetic singlet (S_1) and triplet (T_1) states.[1–3] As a result, TADF permits 100% internal quantum efficiency (IQE), outperforming the 25% limit of conventional fluorescent emitters and offering a metal-free alternative to phosphorescent counterparts. Many blue TADF-OLEDs now demonstrate external quantum efficiencies (EQE) above 20%, underscoring their promise for advanced displays and illumination applications.[4,5] Nonetheless, efficiency roll-off at practical luminance levels and operational lifespan of blue TADF-OLEDs continue to hinder their broad commercialization despite intense research on donor–acceptor (D–A) and multi-resonant (MR)-TADF emitters and hyperfluorescent architectures.[3,5,6] While research has increasingly prioritized lifetime improvements, many studies still neglect detailed stability assessments, highlighting the urgency for consistent reporting to accelerate progress.[7,8]

The fundamental difficulty for blue devices is the high energy of singlet and triplet excitons in the emissive layer. Under electrical operation, long-lived triplets and high exciton and polaron densities promote multi-excitonic and charge-assisted processes that generate even higher-energy "hot" excited states.[7,9,10] When these exceed the bond dissociation energies (BDEs) of the weakest bonds, irreversible bond cleavage, defect formation and non-radiative recombination sites are created, leading to luminance decay and voltage rise.[11,12] At the same time, organic materials are intrinsically less stable in their ionized states, so strong electron or hole injection into chemically fragile motifs accelerates degradation. These effects are especially severe in blue TADF-OLEDs, where triplet energies above 2.8–3.0 eV are required.[13,14]

While numerous TADF emitters have been engineered with improved photostability,[3,9,14,15] systematic lifetime-oriented

[a] Institute of Photonics and Nanotechnology, Faculty of Physics, Vilnius University, Saulėtekio av. 3, LT-10257 Vilnius, Lithuania. E-mail: karolis.kazlauskas@ff.vu.lt
[b] Department of Polymer Chemistry and Technology, Faculty of Chemical Technology, Kaunas University of Technology, Barsausko 59, LT-51423, Kaunas, Lithuania

studies on high-triplet-energy hosts lag behind,[16–18] even though hosts dominate the emissive-layer volume. High-triplet-energy hosts such as mCBP, mCP, DPEPO and their derivatives are widely used, but their triplet energies lie close to the dissociation thresholds of common organic bonds, making them vulnerable to hot-exciton and polaron-induced damage.[10,19,20] Mixed-host, exciplex-forming and TADF-host architectures have been explored to broaden the recombination zone, balance charge transport and manage triplet populations.[21–24] However, the microscopic connection between host structure, charge-transport character, bond strength and device stability is still poorly understood. Thus, there is a clear need for controlled studies in which host structure is varied in a targeted manner, while keeping device architecture and emitters fixed, enabling direct correlations between intrinsic host robustness and operational stability. This is rarely done in the literature on blue TADF-OLEDs, where changes in emitters, hosts and device stacks are often coupled.[7,8,25,26]

To this end, in this work, we develop a series of carbazole–biphenyl hosts whose structures are tuned to enhance electron transport while retaining high triplet energies compatible with blue TADF emitters. The series varies from a weakly hole-transporting, nearly ambipolar host to strongly electron-transporting analogues, allowing us to probe how charge balance affects efficiency roll-off and lifetime. Using blue TADF emitters of different triplet energies and doping levels, we examine exciton confinement and host–guest energy transfer. We then combine device characteristics with thermal analysis, photoluminescence studies, and quantum-chemical calculations of the weakest exocyclic C–N bond dissociation energies in various charge states. By linking C–N bond strength in the hosts to device performance, we aim to establish chemically grounded design principles for robust, high-triplet-energy hosts tailored for blue TADF-OLEDs. Ultimately, this study prioritizes a systematic comparative evaluation of host influences on device performance, particularly stability, rather than solely targeting peak device metrics.

2. Experimental

2.1. Materials

All reagents and chemicals were purchased and used as received unless otherwise noted. Solvents were distilled and degassed prior to use. 9-Ethylcarbazole and bis(triphenylphosphine)palladium(II) dichloride ($PdCl_2(PPh_3)_2$) were purchased from Sigma-Aldrich. *N*-Bromosuccinimide (NBS), 3-bromo-9*H*-carbazole, 1,4,7,10,13-pentaoxacyclopentadecane (15-crown-5), 3-fluorobenzonitrile, potassium carbonate (K_2CO_3), cesium carbonate (Cs_2CO_3) were obtained from Fluorochem. Sodium *tert*-butoxide (*t*-BuONa), 3,3′-bis(4,4,5,5-tetramethyl-1,3,2-dioxaborolan-2-yl)-1,1′-biphenyl, and 2,2′-bis(4,4,5,5-tetramethyl-1,3,2-dioxaborolan-2-yl)-1,1′-biphenyl were purchased from TCI. 6-Bromo-9-ethyl-9*H*-carbazole-3-carbonitrile was synthesized according to the previously reported procedure.[27]

2.2. Methods

All reactions were performed under an inert atmosphere (N_2 or Ar). Reaction progress was monitored by TLC on silica gel 60 F254 aluminum plates (Sigma-Aldrich) with UV visualization. Column chromatography employed silica gel 60 (particle size 0.063–0.20 mm). ^1H and ^{13}C NMR spectra were acquired on a Bruker Avance III (400 MHz and 101 MHz, respectively) in $CDCl_3$ with tertamethylsilane (TMS) as an internal standard. Chemical shifts (δ) are reported in ppm. Mass spectra (MS) were recorded on a Waters SQ Detector 2; the compounds were dissolved in 1 : 1 MeOH/MeCN. The final synthesized products were purified by vacuum sublimation. Thermogravimetric analysis (TGA) was carried out on a TA Instruments Q50 under N_2 from 0 to 800 °C at 20 °C min^{-1}. Differential Scanning Calorimetry (DSC) was performed on TA Instruments Q2000 at 10 °C min^{-1}.

Optimization of ground state geometries was performed in toluene using density functional theory (DFT) with the B3LYP functional and the 6-31G(d) basis set, as implemented in Gaussian 09W software. The energies of the first singlet and triplet excited states, oscillator strengths, and highest occupied molecular orbital (HOMO) and lowest unoccupied molecular orbital (LUMO) of the investigated compounds were calculated using the Tamm–Dancoff approximation (TDA) within time-dependent DFT (TD-DFT) at the B3LYP/6-31G(d) level in toluene, based on the optimized ground-state geometries. BDEs were calculated at the same basis set level for neutral, cationic and anionic states by running geometry optimization of intact molecule and its dissociated species.

Absorption spectra were measured using a UV-vis-NIR spectrophotometer, PerkinElmer Lambda 950. Neat films were prepared by spin-coating $CHCl_3$ solutions (10 mg mL^{-1}) on quartz at 2000 rpm; 1 wt% PMMA films were prepared by drop-casting toluene solutions (80 mg mL^{-1}). Films were annealed (neat: 50 °C; PMMA: 100 °C) for 15 min to remove residual solvent. Steady-state photoluminescence (PL) spectra were recorded using a Hamamatsu PMA-12 back-thinned CCD, with a xenon lamp coupled to a monochromator as the excitation source, exciting at the absorption maxima. Film PL quantum yields (PLQY) were determined in an integrating sphere (SphereOptics) following the de Mello integrating-sphere protocol for absolute PLQY of thin films.[28] Solution FL transients were measured at 400 nm by time-correlated single photon counting (PicoQuant; PicoHarp 300) utilizing 340 nm pulsed diode laser (repetition 1 MHz, pulse width 600 ps). Film FL transients were measured with YAG:Nd^{3+} laser Ekspla NT 242 (OPO at 300 nm, 5 ns, 1 kHz) and a time-gated iStar DH340T ICCD (Andor) mounted on a Shamrock SR-303i spectrograph. Low temperature measurements were performed using a closed-cycle He cryostat (Cryo Industries 204N).

Cyclic voltammetry (CV) was performed with an eDAQ 466 potentiostat in a three-electrode cell (glassy carbon working, Pt/Ti counter, Ag/AgCl reference) in N_2-purged DMF containing 0.1 M *n*-Bu_4NBF_4 at 2.0 mM analyte concentration and 100 mV s^{-1} potential scan rate. Potentials were referenced to the Fc/Fc^+ redox couple measured under identical conditions; energy levels were converted relative to vacuum using the common −4.8 eV offset for Fc/Fc^+.

Patterned ITO/glass substrates (Kintec) employed for the fabrication of OLEDs were sequentially sonicated in Hellmanex

II, deionized water, acetone, and isopropanol, then treated with O_2 plasma (10 min). Substrates were transferred into a multichamber thermal-evaporation system (base pressure $<1 \times 10^{-6}$ Torr) housed in a N_2 glovebox. A stack of organic layers was deposited at a rate of ~ 1 Å s^{-1}; thicknesses and rates were monitored using a quartz crystal microbalance. Without breaking the vacuum, LiF and Al were deposited at 0.2 and 1 Å s^{-1}, respectively. The device active area was 2×2 mm^2 (defined by the ITO pattern and cathode shadow mask). Finished devices were transferred to the glovebox without exposure to air and encapsulated with a glass lid and UV-curable epoxy (KATIOBOND LP655; DELO).

Electrical–optical characterization of OLEDs employed a calibrated integrating-sphere system (ORB Optronix) coupled to a RadOMA GS-1290 spectroradiometer and a Keithley 2601A source meter. Current–voltage–luminance (*I–V–L*) characteristics, external quantum efficiency (EQE), and efficiency roll-off were measured at room temperature. Device operational lifetimes were measured under constant–current–density drive using a Keysight U2722A source-measure unit, while luminance was monitored with a calibrated silicon photodiode (Thorlabs).

3. Results and discussion

3.1. Synthesis and DFT calculations

We first outline the molecular design and synthesis of the carbazole–biphenyl hosts used in this study (Scheme 1), and summarize their frontier-orbital characteristics from DFT.

Compounds **mCzB-2CN**, **oCzB-2CN**, and **mCzB-2PhCN** were obtained *via* one-step Pd-catalyzed cross-coupling reactions between the corresponding biphenyl bis(boronate) intermediates and bromocarbazole nitriles. The reactions employed $PdCl_2(PPh_3)_2$ as the catalyst and K_2CO_3 or Cs_2CO_3 as the base. Full synthetic procedures and product characterization details are provided in the SI.

DFT calculations show that the HOMOs of all three hosts are extensively delocalized over the entire backbone, indicating efficient π-electron communication between the carbazole groups and the central biphenyl linker (Fig. 1). In contrast, the LUMO shows a clear dependence on the linkage pattern. In **mCzB-2CN** and **oCzB-2CN** it is mainly localized on the cyano-substituted carbazoles, whereas in **mCzB-2PhCN** it shifts toward the N-substituted cyano–phenyl groups, reflecting the altered conjugation pathway introduced by *N*-phenyl substitution. Importantly, the redistribution of LUMO density in **mCzB-2PhCN**, away from the carbazole core and toward the cyano–phenyl moieties, suggests its enhanced anionic-state C–N bond strength discussed in Section 3.6.

These orbital patterns correlate closely with the calculated excitation energies summarized in Table 1. The *meta*-type linkage in **mCzB-2CN** slightly twists the conjugation path, resulting in a singlet energy of 3.8 eV, while the more angular *ortho*-linked geometry of **oCzB-2CN**, with reduced conjugation across the core, marginally raises the S_1 level to 3.83 eV but enhances local excitation character, as evidenced by its larger oscillator strength (f = 0.12). Conversely, in **mCzB-2PhCN** the conjugation extends through the *N*-phenyl substituent and terminates at the cyano–phenyl unit. This increased π-delocalization over the peripheral rings lowers the S_1 to 3.33 eV. Its triplet energy (T_1 = 3.12 eV) is also reduced,

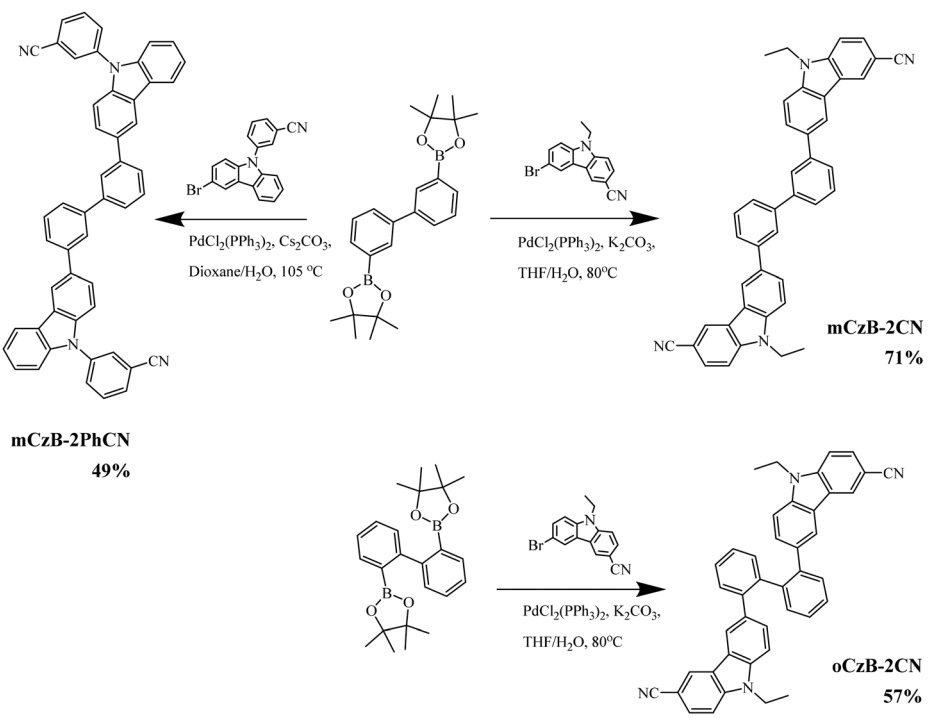

Scheme 1 Synthetic routes to carbazole–biphenyl hosts **mCzB-2CN**, **oCzB-2CN**, and **mCzB-2PhCN**. Isolated yields are indicated.

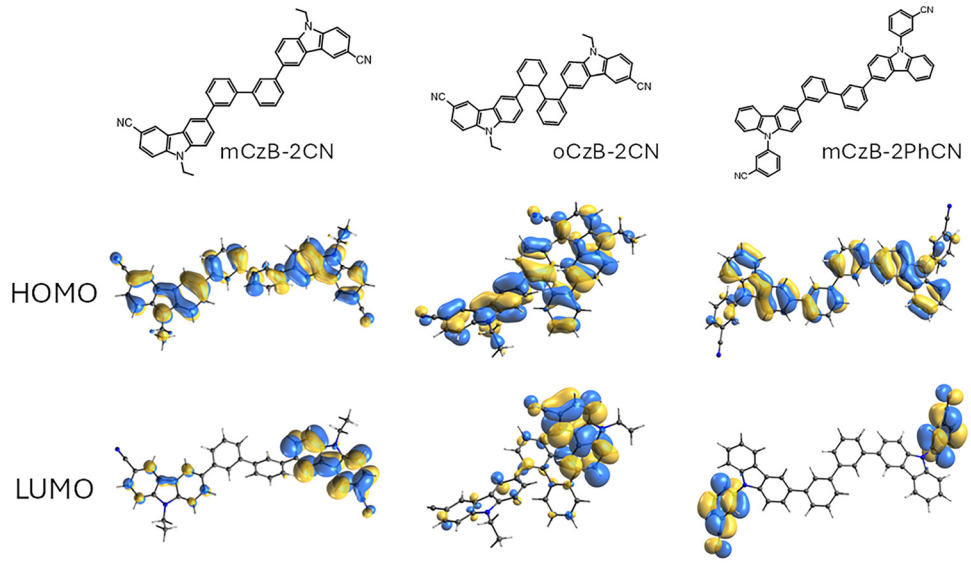

Fig. 1 HOMO and LUMO of the carbazole–biphenyl hosts obtained by DFT B3LYP/6-31G(d) calculations.

Table 1 First singlet and triplet excited-state energies and oscillator strengths of the investigated compounds calculated by TDA of TD-DFT (B3LYP/6-31G(d)) in toluene at optimized ground-state geometry

Compound	S_1 (eV)	f, $S_0 \rightarrow S_1$	T_1 (eV)
mCzB-2CN	3.8	0.041	3.26
oCzB-2CN	3.83	0.120	3.28
mCzB-2PhCN	3.33	0.071	3.12

consistent with the more extensive charge-transfer character of the excited state.

3.2. Thermal and electrochemical properties

Having established the electronic structures of the hosts, we next assessed their thermal robustness and electrochemical energy levels. Thermal analysis by TGA and DSC indicates that all three carbazole–biphenyl-type host materials **mCzB-2CN**, **oCzB-2CN**, and **mCzB-2PhCN** exhibit excellent thermal stability. As shown in Fig. 2a and summarized in Table 2, the temperatures, corresponding to 5% weight loss ($T_{d,5\%}$) of these materials, exceed 390 °C, confirming their suitability for vacuum deposition. The lower $T_{d,5\%}$ of **oCzB-2CN** relative to the *meta*-linked analogues is likely attributed to the sterically hindered *ortho*-linked structure, which enforces a more twisted conformation that may alter solid-state cohesion and volatility, reducing the mass-loss temperature.[29]

Although the DSC thermograms (Fig. S1a–c) reveal distinct melting points for certain compounds, the absence of recrystallization upon cooling indicates good glass-forming ability and, consequently, favorable morphological stability. Additionally, all the materials exhibit high glass transition temperatures (T_g) in the range of 140–148 °C, indicative of rigid molecular backbones and strong intermolecular interactions. Such high T_g values are particularly reassuring for device stability tests at 1000 cd m^{-2}, where Joule heating and prolonged operation can otherwise induce morphological relaxation.

Cyclic voltammetry (Fig. 3) shows quasi-reversible/irreversible reduction and oxidation waves within the electrochemical window of the electrolyte. The oxidation for all three hosts is

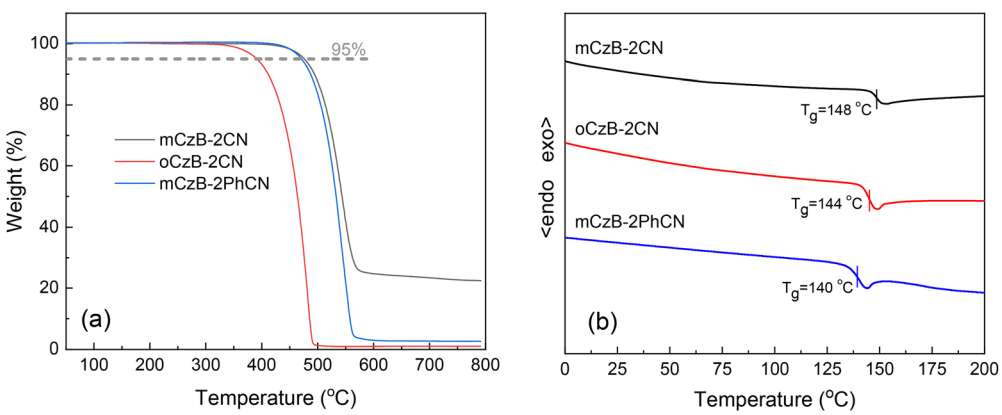

Fig. 2 TGA curves (a) and DSC second heating scans (b) of the carbazole–biphenyl hosts.

Table 2 Thermal properties of the carbazole-biphenyl hosts

Compound	$T_{d,5\%}$[a], °C	T_m[b], °C	T_g[b], °C
mCzB-2CN	476	267	148
oCzB-2CN	391	282	144
mCzB-2PhCN	471	—	140

[a] Measured by TGA under nitrogen atmosphere at a heating rate of 20 °C min^{-1}. [b] Measured by DSC under nitrogen atmosphere at a heating rate of 10 °C min^{-1}.

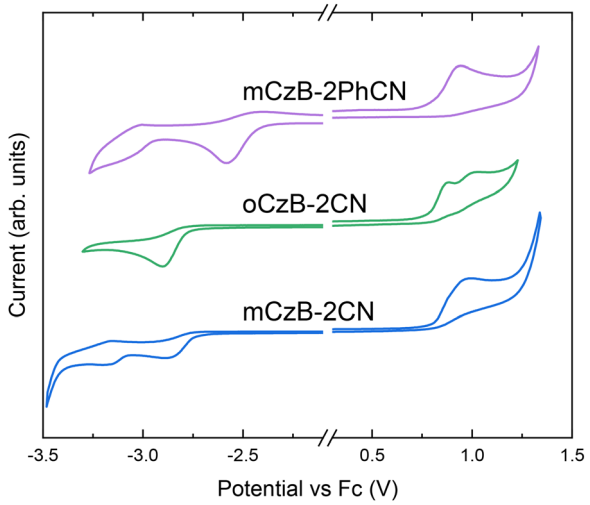

Fig. 3 Cyclic voltammograms of the carbazole–biphenyl hosts.

attributed to the carbazole–biphenyl backbone, with nearly identical onset potentials, giving shallow electrochemical HOMO energies in the −5.67 to −5.62 eV range (Table 3). Cathodic scans exhibit reductions centered on the cyano-bearing termini, yielding deep electrochemical LUMO levels (**oCzB-2CN**: −1.97 eV; **mCzB-2CN**: −2.01 eV; **mCzB-2PhCN**: −2.28 eV, the deepest in the series due to LUMO localization on the *N*-substituted cyano–phenyl units). Accordingly, the electrochemical gaps follow **mCzB-2PhCN** (3.38 eV) < **oCzB-2CN** (3.65 eV) ≈ **mCzB-2CN** (3.66 eV), in line with **mCzB-2PhCN** having the lowest S_1 from TD-DFT.

These findings confirm that adjusting carbazole and biphenyl linkage topology and cyano group position primarily tunes the LUMO, while leaving the oxidation-derived HOMO nearly unchanged. The combination of shallow HOMOs and deep LUMOs suggests favorable alignment with typical charge transport layers, facilitating efficient charge injection in the OLED stack.

3.3. Photophysical properties

To understand exciton confinement and energy transfer in devices, we next examined the photophysical properties of the hosts in solution, dilute films and neat films. The absorption and FL spectra of the studied hosts in dilute toluene solutions (Fig. S2), along with the discussion, are provided in the SI. The absorption spectra of the neat films (Fig. 4) resemble those of the solutions (Fig. S2), albeit with slightly redshifted band profiles. Room-temperature FL of the 1 wt% PMMA films is narrowband and structured for all three hosts, with maxima comparable to those recorded in dilute toluene (Fig. S2). The PMMA films emit at slightly higher energy than the corresponding neat films (Table 3), consistent with the red shift and mild broadening induced by aggregation-induced stabilization in the neat state.

At 10 K, the phosphorescence spectra of the 1 wt% PMMA films display the most energetic 0–0 peaks at 415 nm (**mCzB-2CN**), 422 nm (**oCzB-2CN**), and 418 nm (**mCzB-2PhCN**), yielding T_1 of 2.99, 2.94, and 2.97 eV, respectively. In the neat films, the highest-energy phosphorescence peaks are masked by delayed FL originating from TTA. To extract neat-film T_1 values, the phosphorescence spectra of the PMMA films were rigidly shifted to match the neat-film spectra (Fig. S3). This procedure yields T_1 values of 2.85 eV for **mCzB-2CN**, 2.77 eV for **oCzB-2CN** and 2.82 eV for **mCzB-2PhCN**. Notably, the phosphorescence spectrum of **oCzB-2CN** is more red-shifted and broadened, with largely suppressed vibronic structure, compared to **mCzB-2CN** and **mCzB-2PhCN**. Such spectral characteristics are consistent with the formation of intermolecular triplet excimer states, which have been reported for closely related carbazole-based host materials.[30,31] This behavior suggests stronger intermolecular coupling in **oCzB-2CN** relative to the other hosts.

Evaluation of T_1 energies in neat films is crucial for host materials, since in OLEDs the hosts operate in concentrated solid phases where intermolecular coupling can stabilize triplet states and govern exciton confinement. The measured neat-film T_1 energies of **mCzB-2CN** and **mCzB-2PhCN** (2.82–2.85 eV) are comparable to that of the benchmark host mCBP (T_1 ≈ 2.80–2.85 eV),[31,32] confirming their suitability for triplet confinement in typical blue and sky-blue devices, whereas the somewhat lower T_1 of **oCzB-2CN** (2.77 eV) may result in insufficient confinement, depending on the choice of emitter.

Table 3 Photophysical and electrochemical properties of the carbazole-biphenyl hosts in 1 wt% PMMA and neat films

Compound	PMMA 1%[a] S_1, eV	PMMA 1%[b] T_1, eV	Neat[a] S_1, eV	Neat[c] T_1, eV	TOL[d] PLQY, %	HOMO[e], eV	LUMO[e], eV
mCzB-2CN	3.52	2.99	3.43	2.85	21	−5.67	−2.01
oCzB-2CN	3.51	2.94	3.46	2.77	16	−5.62	−1.97
mCzB-2PhCN	3.63	2.97	3.38	2.82	9	−5.66	−2.28

[a] Calculated from the onset of FL spectrum. [b] Energy of the first peak of the phosphorescence spectrum in a 1 wt% PMMA film measured at 10 K. [c] Estimated from the wavelength shift of the phosphorescence spectra between the neat film and 1 wt% PMMA films. Neat film phosphorescence spectrum was measured at 10 K. [d] Measured in toluene solution (10^{-5} M) in air. [e] Estimated from the onset oxidation (HOMO) and reduction (LUMO) potentials measured by cyclic voltammetry with Fc/Fc^+ as internal reference, assuming $E(Fc/Fc^+) = -4.8$ eV *vs.* vacuum; values represent electrochemical estimates of the frontier energy levels.

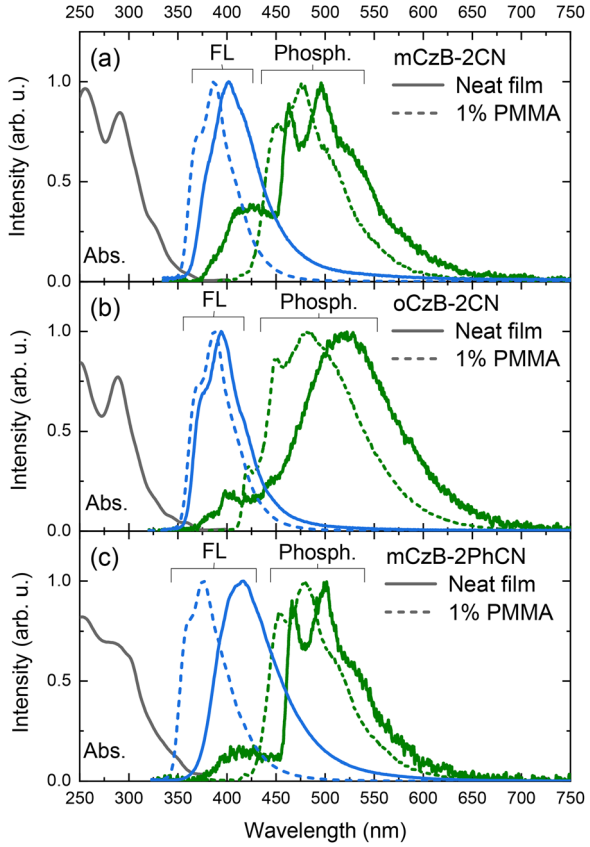

Fig. 4 Absorption (Abs., black), fluorescence (FL, blue), and low-temperature phosphorescence (Phosph., green) spectra of neat films (solid lines) and 1 wt% PMMA films (dashed lines) for (a) **mCzB-2CN**, (b) **oCzB-2CN**, and (c) **mCzB-2PhCN**. Phosphorescence was recorded at 10 K with a 300 μs delay.

FL lifetime measurements of the hosts in solutions, 1 wt% PMMA and neat films showed nanosecond excited-state lifetimes, typical for fluorescent compounds. Full FL transients with the determined decay time constants (Fig. S4), accompanied by a detailed description, are provided in the SI.

3.4. Charge-transport properties and EL device performance

To quantify the charge-transport character of the hosts, hole-only and electron-only devices were fabricated (Fig. 5a and b). The resulting *J–V* curves (Fig. 5c–e) reveal a progression from nearly ambipolar transport in **mCzB-2CN**, with similar currents in HOD and EOD configurations, to increasingly electron-dominated transport in **mCzB-2PhCN** and **oCzB-2CN**. For **mCzB-2PhCN**, the deeper LUMO (−2.28 eV) facilitates electron injection and yields EOD currents about an order of magnitude higher than HOD. Meanwhile, the strongest electron-transporting character of **oCzB-2CN** is attributed to the tighter packing inferred from its photophysical behavior. In devices, this gradual shift toward electron transport is expected to move the recombination zone and modify local exciton and polaron densities, with consequences for both efficiency and stability.

Prior to employing the studied materials as hosts in devices, optimal host:dopant ratios were established. Two previously reported efficient blue TADF emitters, DMeCzIPN (4,6-bis(1-methylcarbazol-9-yl)benzene-1,3-dicarbonitrile)[33] and 4TCzBN (2,3,5,6-tetrakis(3,6-di-*tert*-butyl-9*H*-carbazol-9-yl)benzonitrile),[34] with different triplet energies of 2.79 eV and 2.62 eV, respectively, were selected as dopants. Doping was optimized by monitoring the evolution of FL spectra and PLQY as a function of emitter loading in the hosts (Fig. S5 and Table S1). The good overlap of the neat-film emission of each host with the absorption spectra of both emitters (Fig. 6a) indicates that efficient host-dopant energy transfer should be achievable over the investigated concentration range.

For both emitters, increasing the dopant content leads to gradual quenching of host emission (at ∼400 nm) and a rise in the doped-film PLQY towards a plateau, beyond which further loading brings no significant benefit. On this basis, 7–15 wt% was selected for the higher-triplet emitter (DMeCzIPN) and 40 wt% for the lower-triplet emitter (4TCzBN) as a compromise between efficient energy transfer and minimized concentration quenching. Across the hosts, the *N*-phenylated derivative **mCzB-2PhCN** consistently supports the highest PLQYs at the chosen loadings, whereas the *ortho*-carbazole host **oCzB-2CN** shows reduced PLQY, consistent with its less favorable triplet confinement and possible excimer-like contribution discussed above.

The electroluminescent (EL) devices used to evaluate the hosts were fabricated in the following stack: ITO/HAT-CN (10 nm)/Tris-PCz (30 nm)/Host:Emitter (30 nm)/T2T (10 nm)/BPy-TP2 (40 nm)/LiF (0.8 nm)/Al (100 nm), as summarized by the energy-level diagram in Fig. 6b. The molecular structures of the materials employed in the OLEDs are provided in Fig. S6. In this device configuration, HAT-CN (1,4,5,8,9,11-hexaazatriphenylenehexacarbonitrile) facilitates hole injection into the Tris-PCz (9-phenyl-3,6-bis(9-phenyl-9*H*-carbazol-3-yl)-9*H*-carbazole) hole-transport layer, enabling nearly barrier-free hole injection into the hosts due to well-aligned HOMO levels. The central emissive layer (EML) consists of each host doped with a blue TADF emitter at the predetermined concentration. The compatible HOMO/LUMO of the hosts and emitters (DMeCzIPN: HOMO = −5.67 eV, LUMO = −2.93 eV; 4TCzBN: HOMO = −5.48 eV, LUMO = −2.73 eV; taken from the literature[33,34]) ensured efficient host-to-dopant charge transfer. On the cathode side, T2T (2,4,6-tris(biphenyl-3-yl)-1,3,5-triazine) acts as a hole-blocking layer, while BPy-TP2 (2,7-di(2,2′-bipyridin-5-yl)-triphenylene) functions as the electron-transport layer. This device configuration is widely adopted in high-performance TADF-OLEDs, because it provides balanced carrier injection and tight exciton confinement (depending on the emitter), allowing systematic investigation of how dopant concentration and host identity govern EL properties.[35–38]

Device performance with varied EML compositions is presented in Fig. 7, while the key EL parameters are summarized in Table 4. For broader benchmarking, mCBP-based device data are provided in the SI (Fig. S7 and Table S2). Across all host-emitter combinations, the *J–V–L* and EL profiles confirm blue emission (λ_{EL} ≈ 468–498 nm) and low turn-on voltages (V_{on} = 2.5–3.5 V).

For low DMeCzIPN doping at 7 wt%, the maximum EQE follows the order **mCzB-2PhCN** (13.2%) > **mCzB-2CN** (10.4%) >

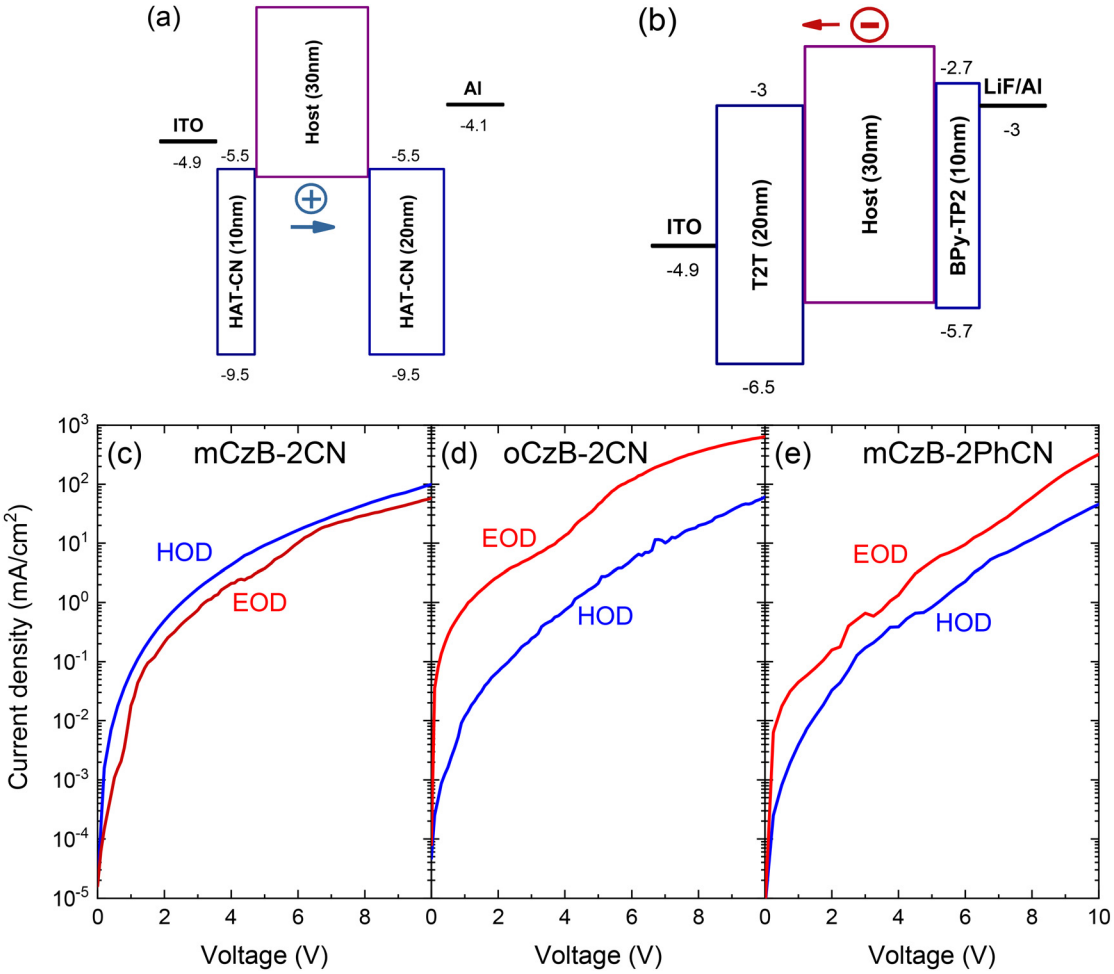

Fig. 5 Single-carrier device characteristics. Energy-level diagrams of (a) hole-only and (b) electron-only devices (energy values in eV), and corresponding current density–voltage (*J*–*V*) curves of (c) **mCzB-2CN**, (d) **oCzB-2CN**, and (e) **mCzB-2PhCN**. HOD and EOD denote hole-only and electron-only devices, respectively.

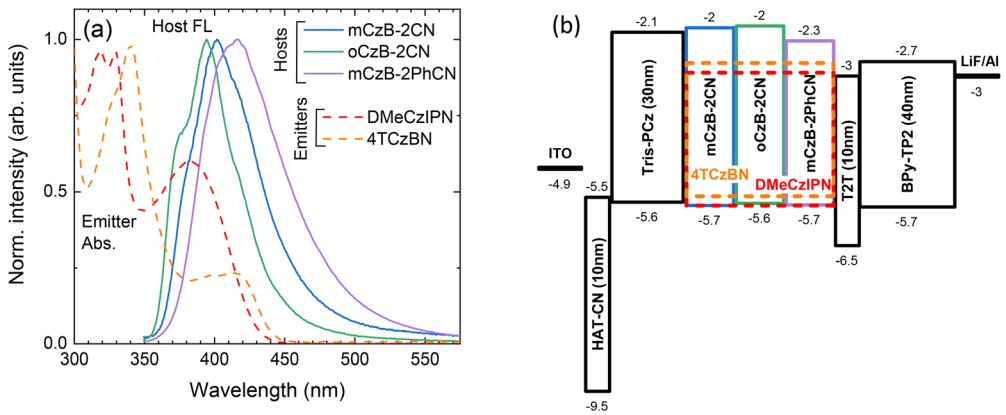

Fig. 6 (a) Absorption spectra of blue TADF emitters (dashed lines) and FL spectra of **mCzB-2CN**, **oCzB-2CN**, and **mCzB-2PhCN** neat films (solid lines). (b) Energy-level diagram of the fabricated TADF–OLEDs using carbazole–biphenyl hosts (**mCzB-2CN**, **oCzB-2CN**, **mCzB-2PhCN**) doped with TADF emitters (4TCzBN and DMeCzIPN). Shown are HOMO/LUMO energies in eV (relative to vacuum) and layer thicknesses in parentheses. Dashed outlines indicate emitter levels within the host layer.

oCzB-2CN (9.6%), with sizable EQE roll-off at 1000 cd m^{-2} of 22%, 20%, and 29%, respectively. The superior performance of **mCzB-2PhCN** is consistent with its higher EML PLQY and favorable electron transport. Conversely, **oCzB-2CN** suffers from

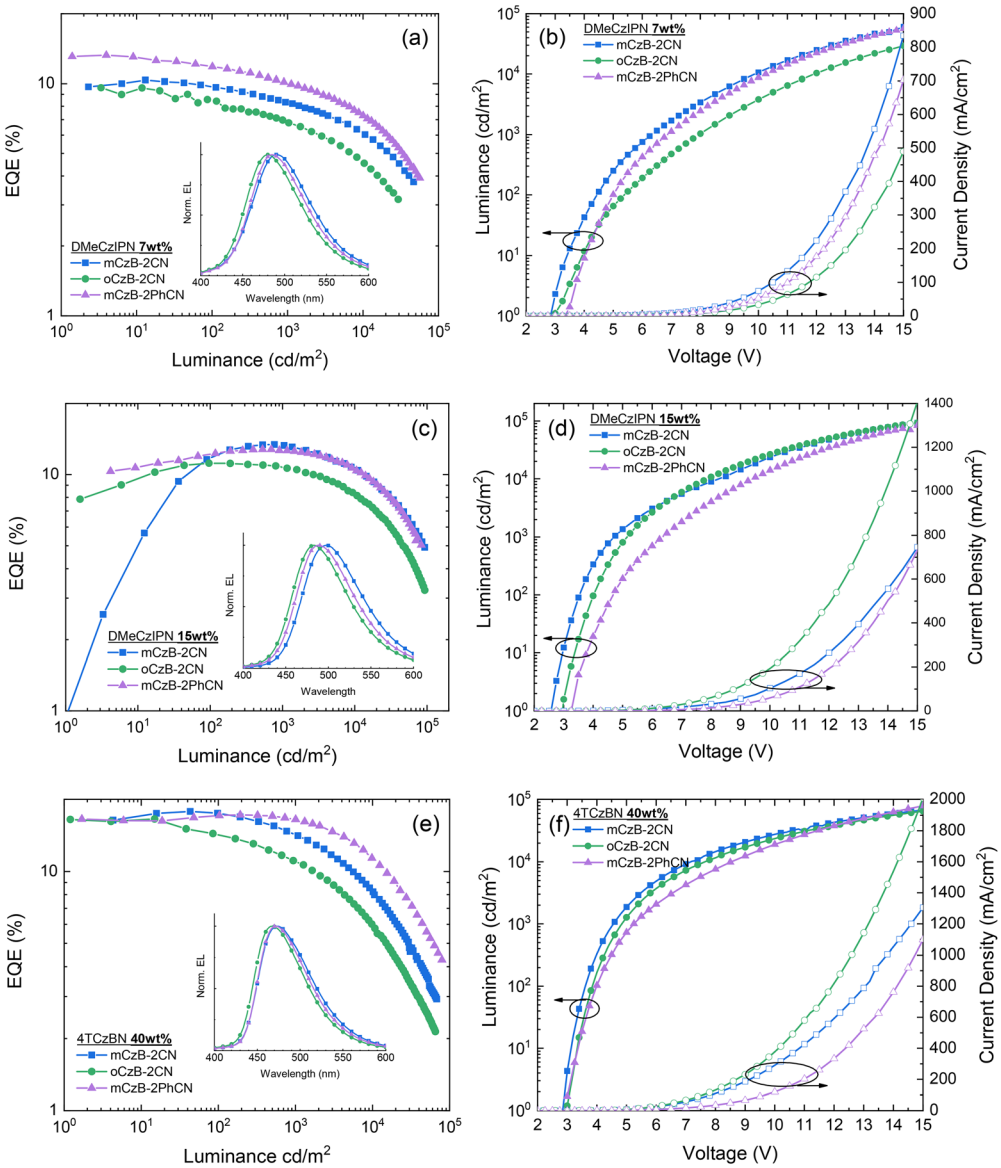

Fig. 7 Performance of blue TADF-OLEDs with varied EML compositions. (a and b) show devices doped with DMeCzIPN (7 wt%), (c and d) with DMeCzIPN (15 wt%), and (e and f) with 4TCzBN (40 wt%) in carbazole–biphenyl hosts. (a, c and e) EQE *vs.* luminance. (b, d and f) *J*–*V*–*L* characteristics: luminance and current density as a function of applied voltage. Insets: Normalized EL spectra for each device set.

Table 4 Main electroluminescence parameters of blue TADF-OLEDs with varied EML compositions

EML	V_{on}[a], V	$V_{@1000cd\,m^{-2}}$, V	EQE_{max}, %	$EQE_{@1000cd\,m^{-2}}$, %	λ_{EL}[b], nm	CIE, (*x*, *y*)	LT_{50}[c], h
mCzB-2CN:DMeCzIPN 7 wt%	2.75	6.5	10.4	8.3	490	(0.18, 0.36)	2
oCzB-2CN:DMeCzIPN 7 wt%	3	8	9.6	6.8	480	(0.17, 0.29)	0.95
mCzB-2PhCN:DMeCzIPN 7 wt%	3.25	7	13.2	10.3	485	(0.18, 0.34)	3.2
mCzB-2CN:DMeCzIPN 15 wt%	2.5	4.75	13.4	13.3	498	(0.21, 0.44)	2.5
oCzB-2CN:DMeCzIPN 15 wt%	3	5.25	11.2	10.6	483	(0.17, 0.33)	2.1
mCzB-2PhCN:DMeCzIPN 15 wt%	3.5	6.5	12.8	12.6	488	(0.18, 0.38)	5
mCzB-2CN:4TCzBN 40 wt%	2.8	4.6	17.9	14.1	473	(0.16, 0.26)	0.55
oCzB-2CN:4TCzBN 40 wt%	3	4.8	16.6	11.1	468	(0.15, 0.21)	0.42
mCzB-2PhCN:4TCzBN 40 wt%	3	5.25	17.3	16.5	472	(0.15, 0.25)	5

[a] Turn-on voltage measured at 1 cd m^{-2}. [b] EL peak wavelength. [c] Device lifetime measured at 1000 cd m^{-2}.

poorer triplet confinement, which introduces additional non-radiative losses and complicates host–guest energy transfer. Together with its less balanced (electron-preferring) transport, these factors promote the strongest roll-off, driven by exciton loss

and undesirable exciton–polaron interactions. See Fig. S8 in the SI for a schematic overview of host–guest transfer/back-transfer considerations and exciton–polaron pathways.

Raising the DMeCzIPN loading to 15 wt% improves host-to-dopant energy transfer and EQE, resulting in **mCzB-2CN** (13.4%) ≈ **mCzB-2PhCN** (12.8%) > **oCzB-2CN** (11.2%), with negligible roll-off for **mCzB-2CN**/**mCzB-2PhCN** (less than 2%) and minor roll-off for **oCzB-2CN** (5%). These results mirror the near-saturated PLQY observed at 15–20 wt% emitter loading and the more favorable carrier balance of **mCzB-2CN** (ambipolar) and **mCzB-2PhCN** (slightly electron-preferring).

With 4TCzBN at 40 wt%, where triplet excitons are strongly confined (T_1 ≈ 2.62 eV) and energy transfer is complete, the devices deliver the highest maximum EQE: **mCzB-2CN** (17.9%) ≈ **mCzB-2PhCN** (17.3%) > **oCzB-2CN** (16.6%). The smallest efficiency roll-off is found for **mCzB-2PhCN** (5%), whereas the largest is recorded for **oCzB-2CN** (33%). The excellent performance of **mCzB-2PhCN** and **mCzB-2CN** reflects stronger triplet localization within the TADF dopant and more balanced charge transport (Fig. 5c and e), which likely broadens the recombination zone and alleviates exciton-mediated quenching.

A modest EQE increase with luminance (up to ~1000 cd m^{-2}) is observed only for DMeCzIPN at 15 wt% (Fig. 7c), attributable to improved carrier balance and a broadened recombination zone under drive.[39,40] At 7 wt% DMeCzIPN (Fig. 7a), incomplete host-to-dopant transfer maintains nonradiative losses and a localized recombination zone, so any bias-induced efficiency gains are offset, and no roll-up is observed. For 4TCzBN at 40 wt% (Fig. 7e), the highly doped EML already achieves near-complete transfer and percolated emitter pathways at turn-on, leaving little room for further improvement. Instead, early-onset TTA/TPA losses and concentration effects keep EQE flat or slightly declining.

These efficiency trends, although important for device performance, do not align with the stability ranking (Section 3.5), pointing out that high efficiency alone is insufficient to predict device lifetime.

3.5. Operational stability and device lifetimes

The stability of the TADF-OLEDs utilizing carbazole–biphenyl hosts was evaluated under constant current driving conditions by measuring the LT_{50} lifetime, defined as the time required for the luminance to drop by 50%. The normalized luminance–time traces, shown in Fig. 8, were recorded at an initial luminance of 1000 cd m^{-2}, a value relevant for practical device applications.[7] For each host–emitter pair, three devices with identical EML compositions were measured, and the resulting LT_{50} values and host stability trends were reproducibly observed.

The device lifetime data consistently reveal a stability ranking of **mCzB-2PhCN** > **mCzB-2CN** > **oCzB-2CN** across all EML formulations (Table 4). With DMeCzIPN at 7 wt%, LT_{50} values follow 3.2 h (**mCzB-2PhCN**) > 2.0 h (**mCzB-2CN**) > 0.95 h (**oCzB-2CN**). Increasing the DMeCzIPN loading to 15 wt% improves lifetimes for all hosts while preserving the order: **mCzB-2PhCN** attains 5 h, whereas **mCzB-2CN** and **oCzB-2CN** remain lower (2.1–2.5 h). Using 4TCzBN at 40 wt% accentuates the difference in LT_{50}: **mCzB-2PhCN** reaches 5 h, while **mCzB-2CN** and **oCzB-2CN** are significantly limited to 0.55 h and 0.42 h, respectively.

The persistence of this trend with two emitters of distinct T_1 energies (2.79 eV for DMeCzIPN; 2.62 eV for 4TCzBN) indicates that triplet localization on the emitter is not the lifetime-limiting factor. Furthermore, several observations suggest that charge transport is unlikely to dominate the lifetime. Despite the substantial differences in carrier-transporting behavior between **mCzB-2CN** (ambipolar) and **oCzB-2CN** (strongly electron-transporting), their devices are found to exhibit rather similar lifetimes (Fig. 8b and c). Additionally, increasing DMeCzIPN loading from 7 to 15 wt%, which is supposed to improve charge balance due to enhanced transfer, does not affect the stability order. Finally, there is no clear correlation between device efficiency and lifetime: *e.g.*, at 15 wt% DMeCzIPN loading, **mCzB-2CN** shows slightly higher EQE_{max} and

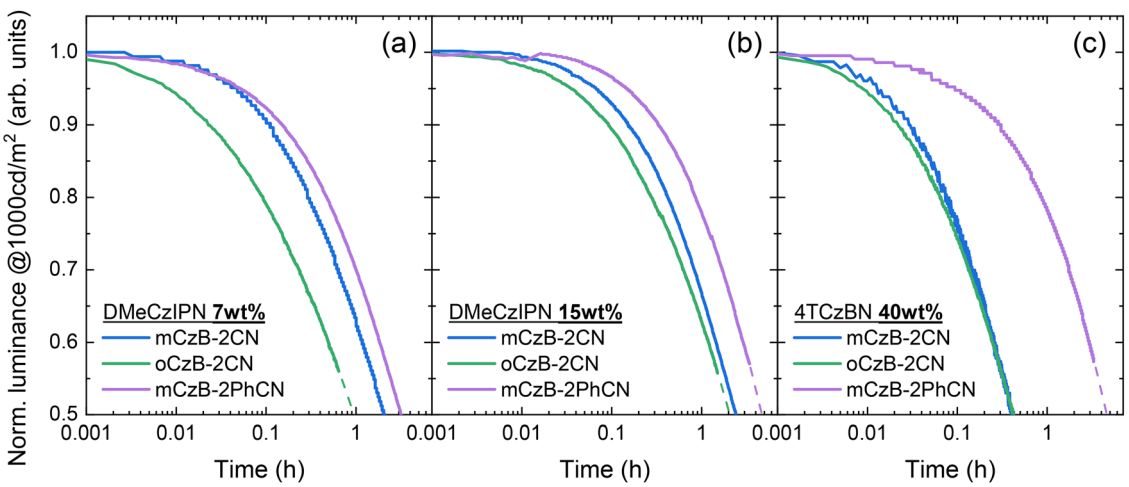

Fig. 8 Operational stability of blue TADF–OLEDs employing carbazole–biphenyl hosts doped with (a) DMeCzIPN (7 wt%), (b) DMeCzIPN (15 wt%), and (c) 4TCzBN (40 wt%). Plots show normalized luminance as a function of time, recorded at an initial brightness of 1000 cd m^{-2}. Devices are compared under identical constant-current driving conditions.

$EQE_{@1000cd\ m^{-2}}$ than **mCzB-2PhCN**, yet its LT_{50} is lower. Considering that the PLQY of the EML is roughly comparable across all hosts at the selected loadings (Table S1), this rules out radiative efficiency as the primary origin of the stability differences.

Taken together, these observations suggest a degradation mechanism that is governed by the intrinsic chemical stability of the host under electrical stress, rather than by macroscopic charge balance or triplet confinement alone.

3.6. BDE analysis of host degradation

To rationalize the host-dependent variations in device lifetime, the intrinsic chemical stability of the hosts was evaluated. To this end, we analyzed the feasibility of bond cleavage *via* bond dissociation energy (BDE) calculations (Table 5 and Table S3). Previous studies have shown that BDEs in the anionic state are particularly informative for OLED stability, especially for fragile C–N linkages, and have introduced the negative charge management as a strategy to suppress electrically driven bond scission.[41] Furthermore, machine-learning approaches to tune exocyclic C–N BDEs and link low anionic BDE to poor material robustness and reduced device lifetime have been applied.[42] Related emitter- and host-focused work has further demonstrated that shifting excitation or charge density away from weak C–N bonds and increasing their anionic BDE can improve operational lifetime.[14,43] However, these trends can be partially masked by differences in charge balance and other material parameters.

Within this context, our DFT calculations identified the exocyclic C–N bond as the weakest linkage in all three hosts, with its stability depending strongly on charge state. In the neutral and cationic manifolds, the lowest C–N BDEs are consistently high (3.2–3.8 eV) for all hosts, implying intrinsic robustness under these conditions. By contrast, the anionic-state BDEs display a large variation, with BDE values dropping to 0.75 eV (**mCzB-2CN**) and 0.73 eV (**oCzB-2CN**), compared to 2.22 eV for **mCzB-2PhCN**. These low anionic BDEs, characteristic of fragile bonds, render the C–N linkage susceptible to scission triggered by exciton–polaron interactions under electrical bias.[44,45] See Fig. S8 in the SI for a schematic depiction linking exciton–polaron interactions to bond scission propensity. The *N*-phenylated host **mCzB-2PhCN** demonstrates a >1.4 eV increase in its weakest anionic BDE relative to **mCzB-2CN** and **oCzB-2CN**, ascribed to its altered LUMO (Fig. 1). Here, electron density is shifted onto the cyano–phenyl substituents rather than the carbazole core, thereby drawing negative charge away from the vulnerable C–N bond and increasing the energy required for homolysis. The anionic-state exocyclic C–N BDE of **mCzB-2PhCN** (2.22 eV) is among the highest values reported for carbazole-based host materials, exceeding most common hosts (typically $\sim$1.3–2.0 eV) and approaching the upper range achieved in charge-stabilized literature designs (Table S4 in the SI).

Table 5 The lowest C–N bond dissociation energies (eV) of carbazole–biphenyl hosts, extracted from Table S3

Host	Neutral	Anion (−1)	Cation (+1)
mCzB-2CN	3.22	0.75	3.67
oCzB-2CN	3.22	0.73	3.45
mCzB-2PhCN	3.64	2.22	3.78

In agreement with design strategies reported for robust OLED materials, wherein stabilizing the anionic state through charge-management or substitution raises BDE and mitigates electrically induced scission,[41,43] the higher anionic BDE of *N*-phenylated host offers a molecular-level rationale for the enhanced operational lifetimes observed in **mCzB-2PhCN**-based devices. Thus, the structural choice of *N*-phenylation in **mCzB-2PhCN** reshapes the LUMO distribution, increases the weakest anionic-state C–N bond, and ultimately manifests as longer device lifetimes.

Although consistent with this broader BDE-based framework, our study extends it to a tightly controlled, high-triplet-energy host platform for blue TADF-OLEDs. The three carbazole–biphenyl hosts form a series in which structural changes (*meta vs. ortho* linkage, *N*-phenylation) primarily reshape LUMO localization and the anionic exocyclic C–N BDE, while triplet energies, thermal stability, and film morphology remain similar. Within a fixed device architecture, and across two blue TADF emitters with different T_1 and multiple dopant loadings, the host stability ranking is invariant and tracks only the anionic-state C–N BDE. This identifies anionic-state C–N bond strength as a practical molecular design parameter for TADF hosts and shows that increasing this bond strength *via* LUMO redistribution (through *N*-phenylation) directly translates into prolonged operational lifetimes in blue TADF-OLEDs.

4. Conclusion

This study adopts a systematic comparative assessment of host effects on device performance in blue TADF-OLEDs, with a particular emphasis on operational stability rather than peak device metrics. It shows that structural tuning at the carbazole and biphenyl units in carbazole–biphenyl hosts modulates LUMO localization and excited-state character while preserving high triplet energies (2.77–2.85 eV in neat films), excellent morphological stability, and thermal robustness. All hosts of the series enable blue TADF-OLEDs with low turn-on voltages and competitive EQEs (up to 18%) when paired with energetically compatible blue TADF emitters, such as DMeCzIPN and 4TCzBN, at optimized doping levels. Operational lifetimes at 1000 cd m^{-2} reach 5 h for the *N*-phenylated host, exceeding those of the non-phenylated analogues by factors of 1.6–12 across devices based on two emitters with different triplet energies and a wide range of dopant concentrations. The consistent stability order under these varied conditions suggests that device lifetime is primarily governed by the intrinsic chemical robustness of the host under electrical stress, rather than by exciton confinement or charge balance alone.

BDE calculations identify the exocyclic C–N bond as the most vulnerable linkage in this host family, showing that only the anionic-state bond strength correlates with the

experimental lifetime trends. Introducing an *N*-phenyl substituent reinforces this bond, enhancing the anionic-state C–N BDE to 2.22 eV (from 0.73–0.75 eV in the non-phenylated hosts) by shifting LUMO density away from the carbazole core, thereby suppressing exciton–polaron–driven cleavage and prolonging operational stability. Therefore, host design for blue TADF-OLEDs should combine high triplet energy, appropriate energy-level alignment, and balanced transport with the elimination or strengthening of weak anionic-state C–N linkages to ensure extended host lifetimes.

Conflicts of interest

The authors declare no conflict of interest.

Data availability

The data that support the findings of this study are available in the supplementary information (SI) of this article. Supplementary information: synthesis, DSC, photophysical data, NMR and MS spectra. See DOI: https://doi.org/10.1039/d5tc04350f.

Acknowledgements

The research was funded by a grant (no. S-MIP-21-12) from the Research Council of Lithuania (LMTLT). E. S. acknowledges funding from the Research Council of Lithuania (LMTLT), agreement No. S-PD-24-73.

References

1 H. Uoyama, K. Goushi, K. Shizu, H. Nomura and C. Adachi, *Nature*, 2012, **492**, 234–238.
2 M. Y. Wong and E. Zysman-Colman, *Adv. Mater.*, 2017, **29**, 1605444.
3 J. M. Dos Santos, D. Hall, B. Basumatary, M. Bryden, D. Chen, P. Choudhary, T. Comerford, E. Crovini, A. Danos, J. De, S. Diesing, M. Fatahi, M. Griffin, A. K. Gupta, H. Hafeez, L. Hämmerling, E. Hanover, J. Haug, T. Heil, D. Karthik, S. Kumar, O. Lee, H. Li, F. Lucas, C. F. R. Mackenzie, A. Mariko, T. Matulaitis, F. Millward, Y. Olivier, Q. Qi, I. D. W. Samuel, N. Sharma, C. Si, L. Spierling, P. Sudhakar, D. Sun, E. Tankelevičiūtė, M. Duarte Tonet, J. Wang, T. Wang, S. Wu, Y. Xu, L. Zhang and E. Zysman-Colman, *Chem. Rev.*, 2024, **124**, 13736–14110.
4 S. O. Jeon, K. H. Lee, J. S. Kim, S.-G. Ihn, Y. S. Chung, J. W. Kim, H. Lee, S. Kim, H. Choi and J. Y. Lee, *Nat. Photon.*, 2021, **15**, 208–215.
5 C.-Y. Chan, M. Tanaka, Y.-T. Lee, Y.-W. Wong, H. Nakanotani, T. Hatakeyama and C. Adachi, *Nat. Photon.*, 2021, **15**, 203–207.
6 K. R. Naveen, P. Palanisamy, M. Y. Chae and J. H. Kwon, *Chem. Commun.*, 2023, **59**, 3685–3702.
7 E. Tankelevičiūtė, I. D. W. Samuel and E. Zysman-Colman, *J. Phys. Chem. Lett.*, 2024, **15**, 1034–1047.
8 Q.-Y. Meng, X.-L. Wen and J. Qiao, *J. Phys. Chem. Lett.*, 2024, **15**, 12571–12583.
9 H. Noda, H. Nakanotani and C. Adachi, *Sci. Adv.*, 2018, **4**, eaao6910.
10 J. Sohn, D. Ko, H. Lee, J. Han, S.-D. Lee and C. Lee, *Org. Electron.*, 2019, **70**, 286–291.
11 S. Scholz, D. Kondakov, B. Lüssem and K. Leo, *Chem. Rev.*, 2015, **115**, 8449–8503.
12 A. S. D. Sandanayaka, T. Matsushima and C. Adachi, *J. Phys. Chem. C*, 2015, **119**, 23845–23851.
13 T. Hatakeyama, K. Shiren, K. Nakajima, S. Nomura, S. Nakatsuka, K. Kinoshita, J. Ni, Y. Ono and T. Ikuta, *Adv. Mater.*, 2016, **28**, 2777–2781.
14 H. Kang, S.-G. Ihn, I. Kim, Y. S. Chung, S. O. Jeon, M. Sim, J. Kim, H. Lee, Y. Son, W.-J. Son, I. Jang, D. S. Kim, H. Choi and J. P. Hong, *Adv. Opt. Mater.*, 2022, **10**, 2102309.
15 S. Jung, W.-L. Cheung, S. Li, M. Wang, W. Li, C. Wang, X. Song, G. Wei, Q. Song, S. S. Chen, W. Cai, M. Ng, W. K. Tang and M.-C. Tang, *Nat. Commun.*, 2023, **14**, 6481.
16 T. H. Ha, J.-K. Bin and C. W. Lee, *Org. Electron.*, 2022, **102**, 106450.
17 S.-G. Ihn, N. Lee, S. O. Jeon, M. Sim, H. Kang, Y. Jung, D. H. Huh, Y. M. Son, S. Y. Lee, M. Numata, H. Miyazaki, R. Gómez-Bombarelli, J. Aguilera-Iparraguirre, T. Hirzel, A. Aspuru-Guzik, S. Kim and S. Lee, *Adv. Sci.*, 2017, **4**, 1600502.
18 S. Y. Byeon, K. H. Lee and J. Y. Lee, *J. Mater. Chem. C*, 2020, **8**, 5832–5838.
19 J. Jiang and J. Y. Lee, *Mater. Today*, 2023, **68**, 204–233.
20 S.-G. Ihn, D. Jeong, E. S. Kwon, S. Kim, Y. S. Chung, M. Sim, J. Chwae, Y. Koishikawa, S. O. Jeon, J. S. Kim, J. Kim, S. Nam, I. Kim, S. Park, D. S. Kim, H. Choi and S. Kim, *Adv. Sci.*, 2022, **9**, 2102141.
21 Z. Wang, C. Wang, H. Zhang, Z. Liu, B. Zhao and W. Li, *Org. Electron.*, 2019, **66**, 227–241.
22 S. J. Park, K. W. Choi, Y. W. Park and B.-K. Ju, *Opt. Mater.*, 2021, **113**, 110879.
23 J. Gu, Z. Tang, H. Guo, Y. Chen, J. Xiao, Z. Chen and L. Xiao, *J. Mater. Chem. C*, 2022, **10**, 4521–4532.
24 Y. Wang, J. H. Yun, L. Wang and J. Y. Lee, *Adv. Funct. Mater.*, 2021, **31**, 2008332.
25 Z. Li, D. Liu and S.-J. Su, *Smart Mater. Dev.*, 2025, **1**, 41402.
26 D. Banevičius, G. Puidokas, G. Kreiza, S. Juršėnas, E. Orentas and K. Kazlauskas, *J. Ind. Eng. Chem.*, 2023, **128**, 515–520.
27 K. R. Justin Thomas, M. Velusamy, J. T. Lin, Y.-T. Tao and C.-H. Chuen, *Adv. Funct. Mater.*, 2004, **14**, 387–392.
28 J. C. de Mello, H. F. Wittmann and R. H. Friend, *Adv. Mater.*, 1997, **9**, 230–232.
29 O. Shalev and M. Shtein, *Org. Electron.*, 2013, **14**, 94–99.
30 S. T. Hoffmann, P. Schrögel, M. Rothmann, R. Q. Albuquerque, P. Strohriegl and A. Köhler, *J. Phys. Chem. B*, 2011, **115**, 414–421.

31 S. A. Bagnich, A. Rudnick, P. Schroegel, P. Strohriegl and A. Köhler, *Philos. Trans. R. Soc., A*, 2015, **373**, 20140446.
32 Q. Xia, Y. Xiang, Y. Gong, S. Li, Y. Wu, Z. Wang and H. Fu, *J. Mater. Chem. C*, 2023, **11**, 6354–6359.
33 G. Kreiza, D. Berenis, D. Banevičius, S. Juršėnas, T. Javorskis, E. Orentas and K. Kazlauskas, *Chem. Eng. J.*, 2021, **412**, 128574.
34 D. Zhang, M. Cai, Y. Zhang, D. Zhang and L. Duan, *Mater. Horiz.*, 2016, **3**, 145–151.
35 H. Fujimoto, S. Kobayashi, H. W. Mo, S. Yukiwaki, K. Nagayoshi, M. Yasumatsu, K. Harada and C. Adachi, *AIP Adv.*, 2018, **8**, 085025.
36 C. H. Park, Y. S. Shim, C. H. Park, S.-G. Jung, Y. W. Park and B.-K. Ju, *Opt. Mater.*, 2018, **86**, 233–238.
37 Y. Tsuchiya, Y. Ishikawa, S.-H. Lee, X.-K. Chen, J.-L. Brédas, H. Nakanotani and C. Adachi, *Adv. Opt. Mater.*, 2021, **9**, 2002174.
38 G. Kreiza, D. Banevičius, S. Juršėnas, F. Rodella, P. Strohriegl and K. Kazlauskas, *Org. Electron.*, 2023, **120**, 106849.
39 N. C. Giebink and S. R. Forrest, *Phys. Rev. B: Condens. Matter Mater. Phys.*, 2008, **77**, 235215.
40 M. Xie, Y. Zhou, L. Zhang, J. Song, C. Ma, Q. Sun, S.-T. Zhang, W. Yang and S. Xue, *Chem. Eng. J.*, 2024, **500**, 156905.
41 R. Wang, Q.-Y. Meng, Y.-L. Wang and J. Qiao, *CCS Chem.*, 2022, **4**, 331–343.
42 Q.-Y. Meng, R. Wang, H.-Y. Shao, Y.-L. Wang, X.-L. Wen, C.-Y. Yao and J. Qiao, *J. Phys. Chem. Lett.*, 2024, **15**, 4422–4429.
43 T. H. Ha, S. W. Kang, J. Y. Yoo and C. W. Lee, *Synth. Met.*, 2024, **303**, 117551.
44 M. Hong, M. K. Ravva, P. Winget and J.-L. Brédas, *Chem. Mater.*, 2016, **28**, 5791–5798.
45 B. van der Zee, Y. Li, G.-J. A. H. Wetzelaer and P. W. M. Blom, *Phys. Rev. Appl.*, 2022, **18**, 064002.

